

pubs.acs.org/cm Article

Ligand Pyrolysis during Air-Free Inorganic Nanocrystal Synthesis

Breena M. Sperry and Christine K. Luscombe*



Cite This: Chem. Mater. 2021, 33, 136-145



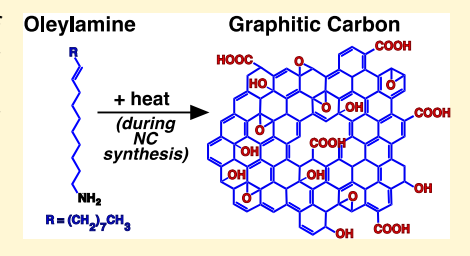
ACCESS I

III Metrics & More



Supporting Information

ABSTRACT: Oleylamine (OLA) is a ubiquitous organic ligand used in the synthesis of inorganic nanocrystals (NCs) due to its ability to reduce metal precursors and sterically stabilize NCs. However, attempts to thermally remove the ligand from deposited OLA-capped NC films result in ligand pyrolysis, where the organic residue is ultimately embedded into the active material as a carbon defect. Herein, we investigated the thermal decomposition and restructuring of OLA ligands using a combination of Raman spectroscopy and X-ray photoelectron spectroscopy (XPS), seeking to determine the specific nature of OLA's decomposition and reasons for its ultimate incorporation into a carbon-rich fine-grain layer observed in $\text{Cu}_2\text{ZnSn}(S_{1-x}\text{Se}_x)_4$ (CZTSSe) systems. While



it has historically been expected that OLA pyrolyzes during thermal treatments, this work identifies that OLA decomposes into nanostructured graphitic carbon, which is first detectable immediately after the NC synthesis at 225 °C, well before the employment of thermal treatments. These graphitic flakes are further identified as disordered graphene oxide, which segregates from OLA-capped NCs during deposition to assemble into the carbon-rich layer. In identifying that the carbon-rich fine-grain layer originates prior to thermal treatments, we introduce a strategy to partially reduce the presence of this layer by isolating the graphene oxide flakes immediately after the CZTS NC synthesis.

1. INTRODUCTION

Solution-processed conductive nanocrystals (NCs) have been extensively investigated for their tunable functional properties and versatility in a wide range of applications within energy and electronics. 1-3 Because NCs are able to be dispersed in a liquid, they can be assembled into films at much lower temperatures than evaporative or ingot processes, making solution-processed NCs a more cost-effective method of bulk material production. Solution-processed NCs are often produced through one-pot syntheses, a streamlined synthetic technique that has few processing steps and high material utilization. 1-3 Typical one-pot syntheses consist of the reduction of organometallic precursors by a coordinating solvent, often an organic ligand. 1,2,4,5 In addition to operating as a solvent and reducing agent, the ligand can influence the size and shape of NCs and can cap and stabilize the suspension of NCs in compatible organic solvents.4-11

While these capping ligands are critical for the synthesis and deposition of NCs through solution processing, the ligand hinders charge transport between particles, making deposited NC films insufficient for practical devices due to their poor charge mobility. 4,6,12–14 While ligand exchange with conductive organics can be employed, 4,6,12 exchange methods are laborious and have limited scalability. Alternatively, thermal treatments promote ligand desorption and overall NC densification, universally improving conduction throughout the film. Our During heating, the ligand desorbs to free the NC surface for sintering; however, the organic material is not eliminated from the film as expected. 11,12,22,25,26 With sufficient annealing times and temperatures, this process results in a

residual pyrolyzed graphitic carbon fine-grain layer (FGL) underneath an inorganic large-grain layer (LGL). 11,15–25 The impact of the carbon-rich layer on film conduction has been debated, with claims that it impedes carrier transport 27 or is benign. Nonetheless, attempts have been made to reduce the thickness of the carbon-rich layer with limited success. 24,25

A commonality across these observations is the use of the capping ligand oleylamine (OLA), which operates as a high-boiling-point solvent, a reducing agent, and a surfactant that caps and screens NCs from their environment. NCs from their environment. NCs their environment, NCs synthesis, NCs from their environment, NCs synthesis, NCs from their environment, NCs synthesis, NCs from the restructuring of OLA into graphitic carbon has received limited attention.

In this paper, we investigate the pyrolysis of OLA and the residual organic constituents within OLA-capped Cu_2ZnSnS_4 (CZTS) NC films and their sintered $Cu_2ZnSn(S,Se)_4$ (CZTSSe) counterparts. Through the usage of Raman spectroscopy and X-ray photoelectron spectroscopy (XPS), the temperature-driven decomposition and restructuring of OLA are assessed. Moreover, XPS and glow discharge optical emission spectroscopy (GDOES) provide insight into a comprehensive model of the ligand's fate during NC

Received: July 27, 2020 Revised: December 5, 2020 Published: December 21, 2020





processing. By identifying both the decomposition conditions, resulting pyrolyzed structure, and origin of the FGL, a partial strategy to control the carbon layer in sintered NC films is presented.

2. EXPERIMENTAL TECHNIQUES

- **2.1. Oleylamine Decomposition.** Microscope slides (2.5 cm \times 2.5 cm) were sequentially sonicated in distilled water, acetone, and isopropyl alcohol (IPA) for 10 min per wash, and then each substrate was air-dried. In air, substrates were heated to their set point temperature, and then 0.2 mL of technical-grade oleylamine (70%, Sigma-Aldrich) was drop-cast onto the substrate. After 20 min, the substrate was removed from the hot plate and allowed to cool.
- **2.2. Nanomaterial Synthesis.** Copper(II) acetylacetonate (1.5 mmol, 99.99%, Sigma-Aldrich), zinc acetylacetonate (0.75 mmol, 99.995%, Sigma-Aldrich), tin(IV) bis(acetylacetonate) dibromide (0.75 mmol, 98%, Sigma-Aldrich), elemental sulfur (99.98%, Sigma-Aldrich), and technical-grade oleylamine (70%, Sigma-Aldrich) were used in the synthesis of Cu2ZnSnS4 NCs. For the oxygen-free reaction, anhydrous CuCl₂ (1.5 mmol, 99.995%, Sigma-Aldrich), anhydrous ZnCl₂ (0.75 mmol, 99.995, Sigma-Aldrich), and anhydrous SnCl₂ (1.5 mmol, 99.99%, Sigma-Aldrich) substituted the acetylacetonate precursors. The metal precursors were sealed in a 100 mL three-neck round-bottom flask in an inert (N2) atmosphere in a glovebox. Upon transfer to a Schlenk line, 10 mL of OLA was injected into the flask and heated at 130 °C by a heating mantle, forming a blue solution. The solution was vigorously mixed and cycled between vacuum and N2 for 1 h, until there was no bubbling under vacuum. Under N2, the solution was heated to 225 °C and immediately injected with 3 mL of a separately prepared sulfur-oleylamine solution (1 M sulfur in oleylamine, mixing at 50 °C for 1 h under air). NC nucleation was initiated by the injection of the sulfur-oleylamine solution, as indicated by a rapid change in color from blue to black. After 2 h of mixing at 225 °C, the flask was raised from the heating mantle and allowed to cool to 80 °C. A mixture of 30 mL of IPA and 5 mL of toluene was poured into the flask. The solution was centrifuged at 13.5k rpm for 15 min. Upon decanting the supernatant, sedimented NCs were dispersed in a 2:1 solution of IPA to toluene, where the centrifuging and decanting process were repeated. The residual solvent was removed with a rotovap, forming a final NC powder, referred to as "powdered" NCs. Samples were further dried for 24 h under vacuum.
- **2.3.** Nanocrystal Ink Formation and Thin Film Deposition. CZTS NCs (200 mg) were suspended in 1 mL of toluene and subjected to 1 h of pulsed ultrasonication (10 s ON/5 s OFF) to form an NC ink. Prior to deposition, 2.5 cm \times 2.5 cm substrates of molybdenum-coated soda lime glass (Mo/SLG) were sequentially sonicated in distilled water, acetone, and IPA for 10 min per wash. Each substrate was air-dried and then plasma-cleaned for 5 min. Ten microliters of ink was pipetted onto the cleaned substrates, followed by immediate doctor blading. For uniform coverage, a doctor blading machine was used with a sweeping rate of 50 mm/s and a spacer height of 25 μ m. After 15 min of controlled drying in air, a second layer of ink was deposited (10 μ L), with an adjusted spacer height of 50 μ m. No heat was applied to dry the films.
- **2.4. Selenization.** Sintered CZTSSe films were achieved by incorporating selenium into the system. Se pellets (400 mg) were evenly distributed around two samples in a graphitic box. These samples were loaded into a tube furnace and purged several times, alternating between vacuum and inert Ar (15 min per cycle). Under a constant Ar flow (100 cm³/min) and atmospheric pressure, the tube was heated to 500 °C. The sample was inserted into the furnace for 20 min followed by rapid cooling.
- **2.5. Graphitic Flake Isolation and Dispersion.** CZTS NCs were washed for a third time in IPA and toluene (1:1), and the supernatant was collected. Within 2 weeks, all material had sedimented from the collected supernatant. Photographs of supernatants collected from each subsequent wash are provided in Figure S5. Without perturbing the sedimented material, the top solvent was

- pipetted off and the remaining solvent was removed with a rotovap, isolating a black powdered material. Isolated material (4 mg) was suspended either in 1 mL of IPA or 1 mL of toluene. To form a dispersion, the material was mixed for 20 min, followed by 20 min of sonication. The dispersions were left to stand for 3 h.
- **2.6. Raman Spectroscopy.** Renishaw InVia Raman Confocal Microscope: an excitation wavelength of 514 nm was used for graphitic carbon, CZTS, and ligand identification. Samples were exposed to a 5–50% maximum laser intensity for 10 s. No background subtraction was used unless otherwise specified. Peak intensities were determined via deconvoluted Gaussian fits.
- **2.7. GDOES.** Horiba GD-Profiler 2: a 4 mm diameter anode was used to ablate films. Plasma conditions and calibrations were modeled after Clark et al. ²¹ Raw GDOES data is given as a function of voltage and time. Cu_2ZnSnS_4 compositional data was calibrated with stoichiometric ratios and calibration factors. The relative spatial depth of the sample can also be extracted from time. For each sample, the first 5 s was excluded due to surface contamination and stabilization. The sample is considered to be fully penetrated once the raw voltage of Mo reached 0.2 V. The resulting *x*-axis is equated to the spatial penetration [%].
- **2.8. XPS.** Surface Science Instruments S-Probe spectrometer: a monochromatized Al X-ray source and a low-energy electron flood gun for charge neutralization were used. X-ray spot size for these acquisitions was $800 \times 800 \ \mu \text{m}^2$. All samples were run as insulators. The pressure in the analytical chamber during spectral acquisition was below 5 \times 10⁻⁹ Torr. The pass energy for survey spectra (composition) was 150 eV. Data analysis was carried out using the Hawk 7 Analysis program (Service Physics, Bend OR). High-resolution XPS spectra were calibrated to the hydrocarbon C 1s peak at 285.0 eV.
- **2.9. Thermal Gravitational Analysis (TGA).** Dynamic TGA was collected from room temperature to 500 $^{\circ}$ C at a heating rate of 10 $^{\circ}$ C/min. A platinum pan was used for all experiments. Sample gas (either air or N_2) was purged at a continuous flow rate of 40 mL/min.
- **2.10.** X-ray Diffraction (XRD). Bruker D8 Discover Microfocus X-ray Diffractometer: Cu K α (λ = 1.54059 Å) radiation was used. A step size of 0.02° 2θ was used to collect the full spectra. Mo COD 9008543 (110) peak center at 40.501° 2θ was used to calibrate the spectra. CZTS COD 2105813 was used for the reference spectra. Lorentzian fit of (112), (200), and (312) planes was used for crystallite size analysis. X-ray spectra and analysis are included in Figure S1.
- **2.11. Transmission Electron Microscopy (TEM).** FEI Technai G2 F20: a 200 kV accelerating voltage and a spot size of 3 were used. The dilute dispersion (10 μ L) was suspended on a 300-mesh copper TEM grid and stored under vacuum overnight. Micrographs are included in Figure S1.
- **2.12.** Scanning Electron Microscopy (SEM) and Energy-Dispersive X-ray Spectroscopy (EDS). FEI Sirion XL30: micrographs were obtained at an acceleration energy of 5 kV and a spot size of 2. Cross-sectional samples were prepared by diamond scribing on the substrate SLG and fracturing the sample. Carbon tape was used to cover as much of the exposed SLG as possible to reduce sample drift and charging. Micrographs are included in Figure S3. Compositional information was collected with an FEI EDS detector. Samples were at a working distance of 5 mm, acceleration energies of 7 and 20 kV with respective spot sizes of 5 and 4 (30–50% dead time, total counts of 1 000 000). Fifty-four spots across nine substrates were collected. Bulk atomic percentages were used to calibrate GDOES compositional data
- **2.13. Profilometry.** Bruker OM-DektakXT Profilometer: a diamond stylus with a 2 μ m radius tip was installed to measure the sample thickness of scribed deposited CZTS films.

3. RESULTS AND DISCUSSION

3.1. Thermal Decomposition of Oleylamine. Throughout OLA's life cycle, the ligand is exposed to several high-temperature processes, including NC synthesis (225 °C),

annealing (100–300 $^{\circ}$ C), and sintering (500 $^{\circ}$ C). To understand how OLA thermally decomposes, the ligand was incrementally heated from 100 to 500 $^{\circ}$ C in the absence of CZTS NCs (Figure 1). No change in OLA was observed until

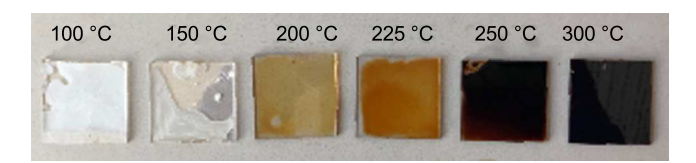


Figure 1. From left to right: OLA annealed on microscope slides at 100, 150, 200, 225, 250, and 300 °C. 0.2 mL of OLA per substrate, each heated for 20 min in air.

150 °C when partial evaporation was observed, despite the temperature being well below the ligand's boiling point of 348 °C. Volatilization at this temperature is likely due to lowboiling-point impurities within technical-grade OLA such as short-chain alkylamine moieties and nitroalkanes.³⁷ OLA cooled from 100 and 150 °C formed a waxy white surface film, attributed to saturated hydrocarbon impurities, which solidify at room temperature.³⁷ At 200 and 225 °C, the film emitted smoke and transformed into an orange-brown liquid. Increased smoking may have resulted from bond cleavage at OLA's allylic bond, leading to lower-molecular-weight hydrocarbons that readily evaporate at these temperatures.3 Furthermore, upon cooling these films, no additional colorimetric change transpired, signifying that irreversible structural decomposition had occurred. Above 250 °C, the films formed a glassy black-brown solid with high opacity. Above the ligand's boiling point (>400 °C, not pictured), the material rapidly vaporized and combusted, leaving little residual material in agreement with previous works.1

To investigate the structural transformation of OLA during pyrolysis, Raman spectroscopy was performed (Figure 2). The

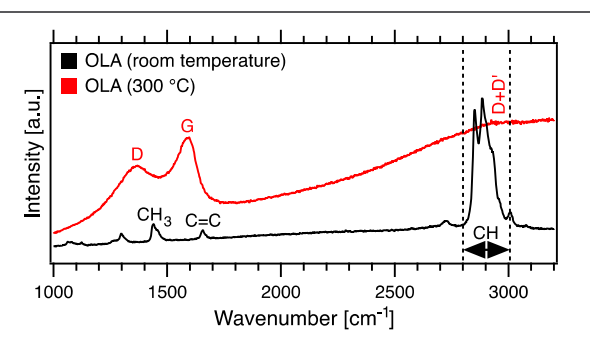


Figure 2. Raman spectra of room-temperature OLA (black) and OLA annealed at 300 $^{\circ}$ C (red). Corresponding identifiable peaks are labeled.

resulting room-temperature spectrum is consistent with the literature, with marked bands that identify the ligand's terminal group (CH₃ bending vibrations at 1439 cm⁻¹), unsaturated bond (cis C=C bending vibrations at 1656 cm⁻¹), and hydrocarbon backbone (C–H stretching vibrations from 2800 to 3006 cm⁻¹). When the ligand was heated to 300 °C, corresponding to the fully darkened structure shown in Figure 1, no residual OLA was detected; rather, graphene's in-plane vibrational mode (G at 1588 cm⁻¹) was observed and accompanied by a disorder (D at 1366 cm⁻¹) and second-order band (D + D' at 2944 cm⁻¹). ^{39–43} The predominant D

band, low D + D' signal, absence of signature second-order bands (2D at 2717 cm $^{-1}$), overall peak attenuation, and fluorescent background are all indicative of the formation of highly disordered graphene, functionalized graphene, or a graphitic carbon system with submicron order. The formation of nanocrystalline graphitic flakes corresponds well with the calculated crystallite size of 6.44 nm, as determined by the Tuinstra and Koenig relation (1) 41,43,48,49

$$L_{\rm a}$$
 (crystallite size) = $C(\lambda) \times \frac{I_{\rm G}}{I_{\rm D}}$ (1)

The crystallite size is a function of the relative fit intensities between the G and D peaks $(I_{\rm G}/I_{\rm D})$ and is proportionate to $C(\lambda)$, an empirical constant found to be 4.4 nm for 514 nm excitation wavelengths. This result is in correspondence with the graphitic carbon found within sintered NC films; however, the onset of decomposition as observed within Figure 1 is the lowest known reported temperature of OLA ligand pyrolysis.

While OLA has been used to intercalate for graphitic carbon systems, 28,50 the formation of graphitic carbon from the pyrolyzed OLA has not been previously reported. Graphite, graphene, and graphene oxide have been produced through pyrolysis of short-chain hydrocarbons; however, this is achieved through epitaxial growth on crystalline substrates that requires temperatures exceeding 900 °C. 51-53 More appropriately, low-temperature multistep carbonization initiated from pyrolytic condensation of OLA may have occurred. 54-57 While this has not been previously reported for OLA, condensation through the formation of nanostructured (<2 nm) polycyclic aromatic hydrocarbons (PAHs) is plausible. PAHs form from allylic cleavage, yielding an alkyl radical and a terminal double bond, which participate in intermolecular cyclization.^{38,58} As OLA contains an allylic site, the ligand likely undergoes similar decomposition, enabling OLA-based carbonization to form the observed ~ 6 nm graphitic carbon flakes.

3.2. Graphitic Carbon Formation during CZTS Nanocrystal Processing. Graphitic carbon has consistently been first detectable within CZTS NC films sintered at 500 °C, 11,15,17,19,34,59 a significantly higher temperature than that required to pyrolyze OLA. This alludes to the possibility that the graphitic carbon formation begins far before the NC sintering as reported in the literature; rather, the ligand may restructure as early as the CZTS NC synthesis at 225 °C. As such, a Raman spectrum of postsynthesized powdered CZTS NCs capped with OLA is presented in Figure 3.

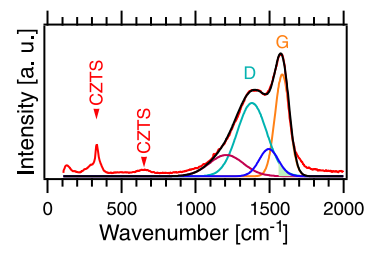
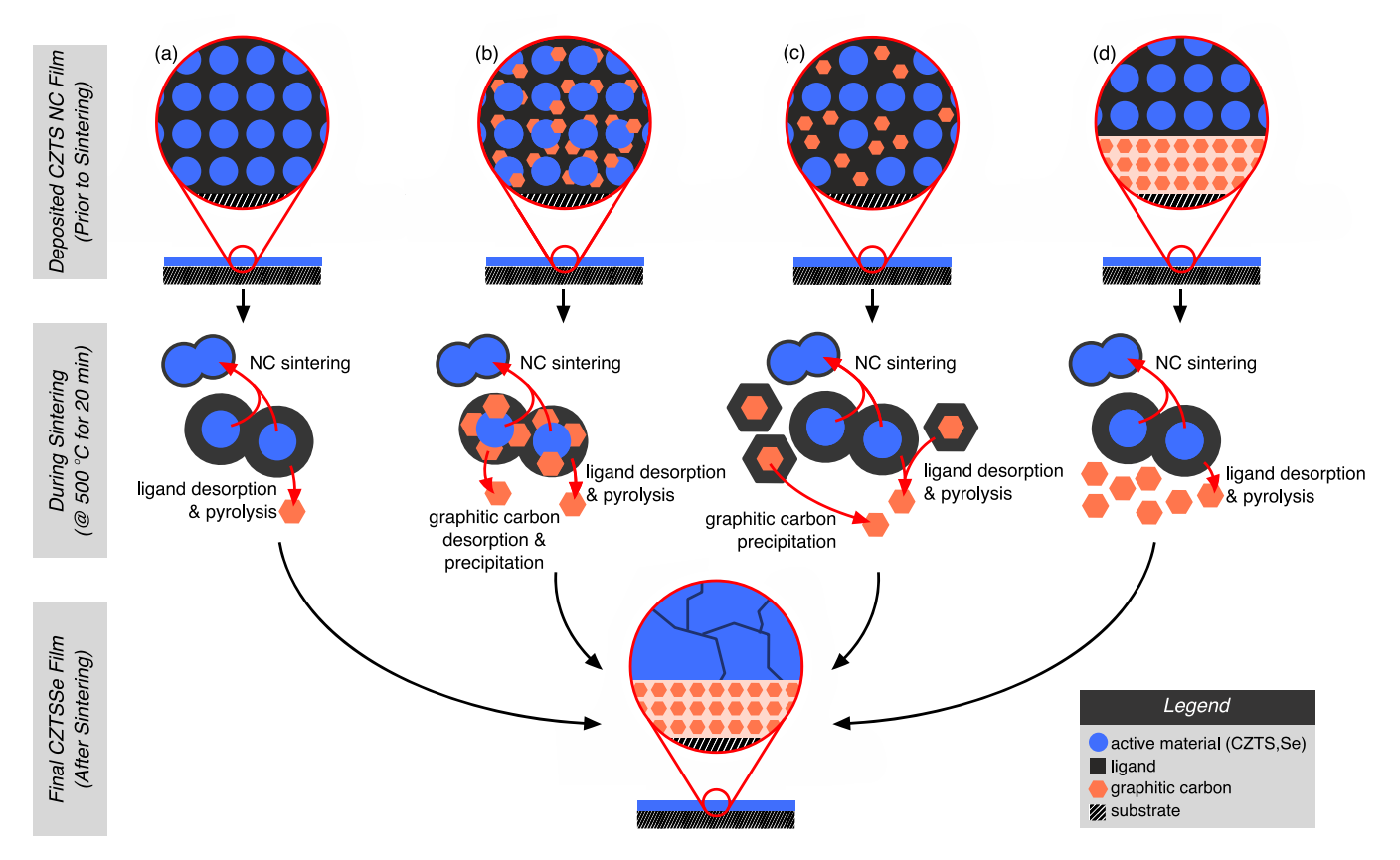


Figure 3. Raman spectrum of powdered CZTS NCs with a focus on the graphitic carbon region. CZTS peak and graphene D and G peaks are labeled. A four-point linear background subtraction was used to eliminate fluorescence.

Scheme 1. Simplified (a) Traditional Model of NC and Grain Growth Account for Ligand Desorption and Pyrolysis during Sintering. Alternative Models Include the Presence of Graphitic Carbon at the Time of Deposition. This Includes (b) CZTS NCs Capped with OLA and Graphitic Carbon, (c) Homogeneous Mixture of OLA-Capped NCs and OLA-Functionalized Graphitic Carbon, and (d) Heterogeneous Mixture of OLA-Capped NCs and Graphitic Carbon^a



^aAll models result in a large-grain layer of the active sintered material above a fine-grained graphitic carbon layer.

In addition to the CZTS signature peak at 338.5 cm⁻¹ and second-order band at 660 cm⁻¹, both the D and G bands were detected at 1379 and 1585 cm⁻¹, respectively. The presence of the D and G bands within powdered CZTS NCs is distinct and verifies that the ligand is restructuring to form the graphitic carbon material during NC synthesis. Furthermore, these bands were, respectively, red- and blue-shifted due to an uptake in structural defects. ^{11,41,42} Deconvoluted left-edge band tailing associated with disordered graphite (1200 cm⁻¹) and an amorphous carbon network (1400 cm⁻¹) was also pronounced. ^{35,60} This rise in defects and amorphous nature can be attributed to metal ions and NCs complicating the formation pathway of graphitic carbon, presumably resulting in an overall less conductive carbon material. ¹¹

Moreover, as calculated via eq 1, the graphitic carbon flakes produced during the CZTS synthesis are also nanometer-scaled, with an approximate crystallite size of 6.12 nm. TEM images (see Figure S1) reveal that the graphitic flakes are comparable in size to the NCs, which ranges from 5 to 70 nm, making the NCs indistinguishable from the graphitic flakes through electron microscopy of bulk films (see Figure S2). As such, this reaction byproduct is overlooked within micrographs of deposited NC films. Thus, by measuring Raman spectra at high wavenumbers, this technique is comparatively effective in detecting graphitic carbon within NC blends. This is critical as the decomposition of OLA can occur for comparable NC syntheses.

3.3. Distribution and Structure of Graphitic Carbon within Deposited Nanocrystal Films. Traditional models of the ligand behavior during NC sintering involve desorption, restructuring, and isolation into a residual carbon-rich FGL, ^{11,22,26} as shown in Scheme 1a. ^{11,22,26} From our Raman investigations, we have observed that graphitic carbon is formed even during the synthesis of the NCs, rather than forming solely during the sintering step. Unless able to isolate the graphitic carbon between synthesis and sintering, it is likely that this residual carbon layer will remain unavoidable as nanostructured graphitic carbon is unable to evaporate below the 500 °C sintering temperature. ⁶¹ As such, in understanding the mechanisms of carbon phase segregation within the final sintered film, the evolution of the FGL can be understood or potentially mitigated.

To address this, Scheme 1b-d includes three alternative models that consider the presence of graphitic carbon at the time of deposition. First (Scheme 1b), in conjunction with the stabilizing ligand (OLA), the graphitic material may anchor to the NC surface as an encapsulant.⁶² During the sintering process, both organic materials desorb and migrate toward the substrate, ultimately forming the FGL. Alternatively (Scheme 1c), the graphitic carbon and NCs may exist as a mixture. The graphitic carbon can be functionalized with OLA, ^{28,50} allowing the phase to be dispersed homogeneously in the NC ink, only to segregate during sintering. In either instance, the carbon-based material diffuses toward the substrate during the

sintering process, forming a carbon-rich FGL underneath large grains of the active material. In contrast, if the graphitic carbon forms a heterogeneous mixture that aggregates during deposition (Scheme 1d), the FGL will form prior to sintering. In this case, instabilities between NC and graphitic carbon allow for graphitic carbon isolation without simultaneously removing the capping ligand required for deposition. This can result in an overall reduction of the FGL in sintered films, as much, if not all of the graphitic carbon can be removed prior to sintering.

To evaluate these models, GDOES was used to identify the carbon distribution throughout the as-deposited CZTS NC films (Figure 4) prior to sintering. While progressing through

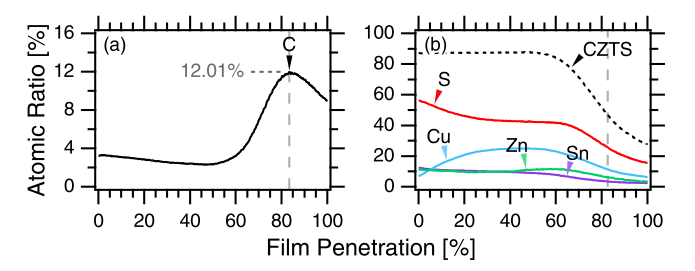


Figure 4. GDOES spectra signifying the spatial composition of (a) CZTS (summation of Cu, Zn, Sn, and S atomic percentages) and (b) carbon. 0% corresponds to the surface of the sample, and 100% indicates substrate penetration (active layer thickness varies from 750 to 1500 nm as determined via a profilometer).

the depth of the film, the concentration of the active material (CZTS) remains consistent across the first two-thirds of the film. Thereafter, the material's concentration rapidly drops off. Within the top half of the film, the concentration of carbon follows the same trend as the active material. However, closer to the substrate, the carbon content reaches an apex immediately after CZTS is diminished. This bimodal distribution of carbon signifies that there is a segregation between the NCs and residual carbon immediately after deposition (i.e., prior to sintering), in agreement with the theory presented in Scheme 1d. It is plausible that the carbon content within the top half of the film arises from the capping ligand, while graphitic carbon settles toward the substrate during the room-temperature drying process. Remarkably, the carbon peak associated with CZTSSe's graphitic FGL (see Figure S3) is spatially consistent with the carbon peak observed in the as-deposited material, further indicating that the graphitic FGL is established prior to sintering or other thermal treatments, such as annealing. However, the chemical nature of carbon throughout the film is indeterminate by GDOES, and, as such, other techniques for exploration of the carbon identity are needed.

The bimodal distribution of carbon-bonding types present within the CZTS film was studied to ascertain whether Scheme 1d is an accurate model. Figure 5 includes XPS data collected on four separate GDOES craters at increasing depths within a CZTS film. Deconvoluted high-resolution C 1s spectra consist of up to four peaks, which represent C=O (~288.5 eV), C-O/C-S (~286.5 eV), C-C sp³ (~285.0 eV), and C=C sp² (~283.7 eV) moieties. Af,63 Intermittent atomic percentage of these moieties and relevant binding modes are quantified in Table 1 (see Figure S4 for full XPS survey spectra and corresponding compositions).

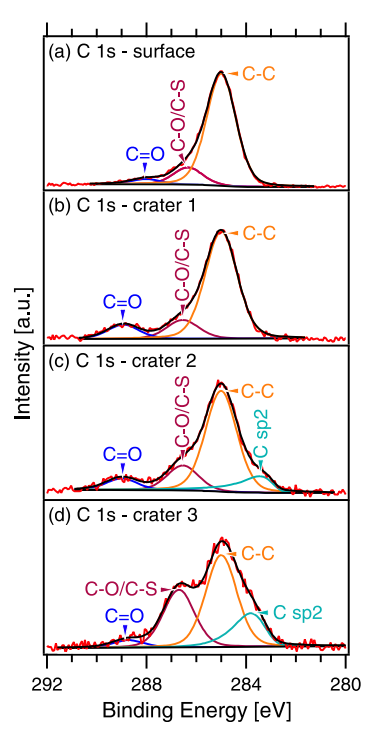


Figure 5. High-resolution XPS spectra on the C 1s peaks of CZTS NC at the (a) sample surface (0% through the film), (b) \sim 25% through the film, (c) \sim 50% though the film, and (d) \sim 75% through the film (in reference to GDOES percentage through the film; Figure 4).

Table 1. XPS Concentration (Atomic Percentages) of Elements of Interest within CZTS NC Samples^a

	surface (%)	crater 1 (%)	crater 2 (%)	crater 3 (%)
C 1s	53.7	30.2	36.2	41.3
C=O	3.9	10.0	7.2	3.9
C-O/C-S	12.8	13.5	15.8	29.9
C-C	83.3	76.5	63.6	47.8
C sp ²	0.0	0.0	13.4	18.4
O 1s	29.4	39.5	44.0	51.8
CZTS	17.0	30.3	19.8	7.0
Cu 2p ₃	14.4	10.8	11.6	17.6
Zn 2p ₃	5.2	31.9	42.2	51.0
Sn $3d_3$	19.6	23.5	13.9	9.8
S 2p	60.8	33.6	32.4	21.6

^aThe total concentrations of carbon (C 1s), oxygen (O 1s) and CZTS (summation of Cu $2p_3$, Zn $2p_3$, Sn $3d_3$, and S 2p) are bolded. The relative concentration associated with carbon bonding (C=O, C-O/C-S, C-C, C sp^2) and CZTS (Cu $2p_3$, Zn $2p_3$, Sn $3d_3$, and S 2p) are included. Full compositional data and parent survey spectra are included in Figure S4.

sp³, C=O, and C-O/C-S binding energies are detectable throughout the bulk of the film. The predominance of sp³ bonding is associated with the ligand's aliphatic backbone. C=O and C-O/C-S bonding are also attributed to the ligand. The conversion of an amine into a C=O containing amide or thioamide (C=S) has been previously been identified during the sulfur mixing in pure octylamines. Similarly, during NC synthesis, C-S bonds originate from ionic sulfur chains, which bridge OLA molecules at their vinyl bonds, forming a polysulfide. This polymerization was qualitatively observed within our reaction by a yellow to red

color change of S in OLA. However, C=O and C-S/C-O likely originate from sources other than the ligand. C=O independently fluctuates throughout the film, and, considering the rise of C-S/C-O despite the decline of S 2p binding energy, C-O bonding likely becomes the predominant moiety in the latter half of the film, mirroring the increase of O 1s.

Variation in composition throughout the film can be attributed to a change in carbon phase. While sp³ bonding associated with the ligand's backbone decreases with film ablation, the overall C 1s carbon concentration mirrors the bimodal carbon distribution as observed in GDOES data. The increase of C 1s is accompanied by the increase of sp² carbon, which is only detectable in the latter half of the film. In agreement with Raman spectroscopy results, the presence of sp² carbon indicates the formation of graphitic carbon from the decomposition of OLA. 47,63 Moreover, XPS data offers further insight into the structure of the graphitic carbon. The presence of C=O and C-O/C-S binding energies and increase O 1s are indicative of graphene oxide (GO). The mutual increase of C-O moieties and sp² is attributed to carboxyl and epoxy groups of GO, 27,47 with additional carbonyl groups stemming from C=0.27,47

The persistence of $\mathrm{sp^3}$ binding and lack of a satellite peak associated with $\pi-\pi^*$ delocalized electrons (between 288 and 293 eV)⁴⁷ signify the formation of nonconductive GO flakes. In addition to $\mathrm{sp^3}$ binding being connected to poor conjugation of GO, $\mathrm{sp^3}$ within the latter half of the film is also associated with the trace amorphous carbon identified in Figure 3. ^{28,63}

3.4. Source of Oxygen. To understand the origin of oxygen within the GO flakes, both the ligand and precursor materials were investigated. If the incorporation of oxygen into the pyrolyzed material stemmed from ligand impurities, such as nitroalkanes as reported by other authors, then it is expected that the ligand will decompose into GO under inert However, as indicated by Raman spectra, as conditions.37 shown in Figure 2, only bonding modes corresponding with the aliphatic alkene are detected. ¹H nuclear magnetic resonance (NMR) of the ligand is in agreement with reference spectra for OLA, with no detection of carbonyl nor amide functional groups (see Figure S6). Further, TGA on the ligand under both air and inert conditions (N2) was performed (Figure 6). During pyrolysis in air, by 225 °C, 63.31% of the material remained, which dropped to 9.24% by 300 °C. This result is in agreement with the decomposition observed in Figure 1, where the ligand is only partially decomposed by 225 °C and heavily pyrolyzed by 300 °C. Under N₂, over 99% of OLA's mass had been lost by 266.1 °C, reflected by the spectra and image on N2-annealed OLA in Figure 6b. This full

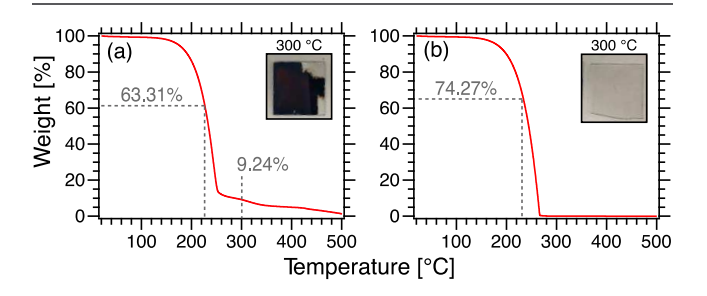


Figure 6. TGA weight loss profiles of OLA both dynamically heated in (a) air and under (b) N_2 . Both figures include a photograph inset of OLA annealed at 300 $^{\circ}$ C under their respective atmosphere.

volatilization of the organic material under inert conditions further signifies that the oxygen source that contributes to GO is not native to the ligand.

As oxygen-containing acetylacetonate precursors were used in the synthesis of CZTS NCs, the oxygen source may be a direct result of precursor selection. To explore the influence oxygen content has on the formation of GO, a chloride-based CZTS NC synthesis was conducted under the same reaction conditions utilized in the acetylacetonate-based synthesis. As shown in Figure 7a, Raman spectra of powdered CZTS NCs

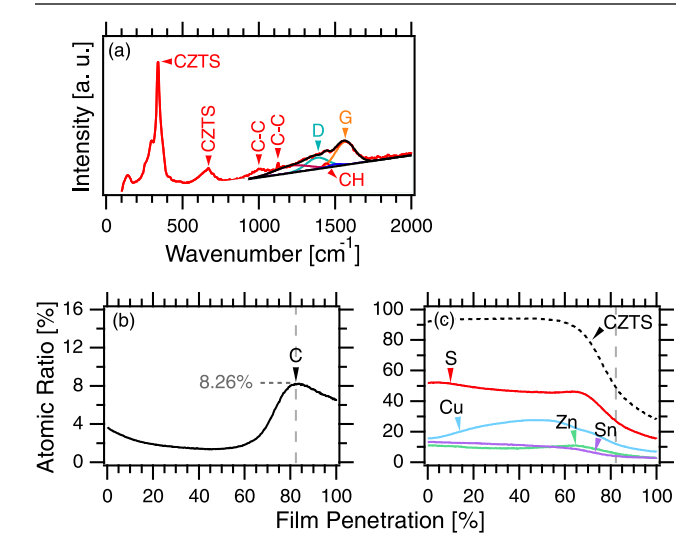


Figure 7. Raman spectrum of (a) powdered CZTS NCs produced via chloride precursors. D and G peaks are identified. GDOES spectra of chloride-based CZTS NC films, which include (b) the film's carbon profile and (c) the film's CZTS profiles (Cu, Zn, Sn, and S).

synthesized with chloride precursors still yield the signature D and G bands of graphitic material. However, the overall intensity of these peaks is diminished in comparison to that observed for acetylacetonate-based reactions. The presence of amorphous material, as indicated by the broad peak at 1200 cm⁻¹, is further evidence that some structural decomposition of the organic material has occurred, but the resulting pyrolyzed material is less graphitic and more amorphous in nature. Additional signals corresponding to the original OLA ligand are detectable, as highlighted by the C-C and C-H bonding modes in Figure 7a. As such, it is apparent that less structural decomposition of OLA occurred for chloride-based syntheses, albeit some graphitic material did form. Nonetheless, GDOES of deposited chloride-based CZTS NC films results in the formation of a carbon-rich layer (Figure 7b), comparable to that observed for acetylacetonate-based CZTS NCs (Figure 4a), in compliance with Scheme 1d. The formation of this carbon layer suggests that the amorphousgraphitic material still forms a heterogeneous dispersion with the CZTS NCs.

The persistence of this carbon layer despite the lack of oxygen sources during the synthesis of CZTS NCs indicates that the formation of pyrolyzed OLA byproducts is not solely contingent on the presence of oxygen. This is observed through the ligand pyrolysis that occurs during the selenization of CZTS NC films at temperatures exceeding 500 °C under inert conditions; 11,22,26 thus, the decomposition of OLA cannot be entirely dependent on oxygen; rather, the formation of graphitic carbon is aided by oxygen. Other external factors

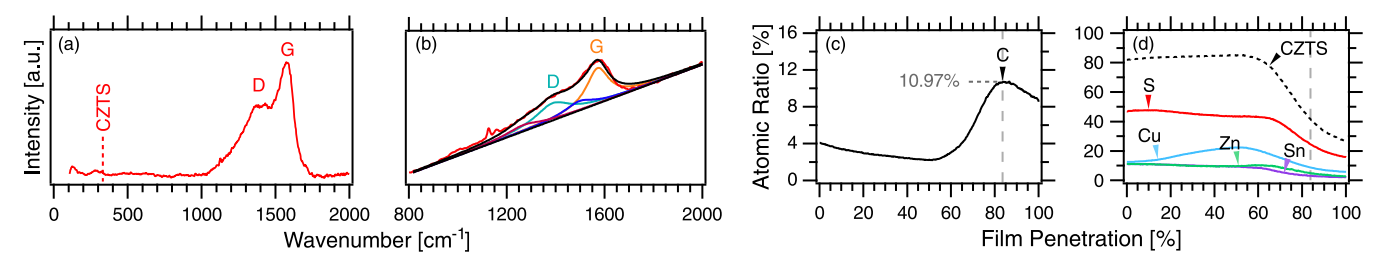


Figure 8. Raman spectrum of (a) powdered supernatant material after subsequent washes. CZTS peak labeled is absent, while D and G peaks are identified. (b) Raman spectra of powdered CZTS NCs (focused on D and G bands) that had been washed three times. GDOES spectra of CZTS NC films that had been washed three times, which include (c) the film's carbon profile and (d) the film's CZTS profiles (Cu, Zn, Sn, and S).

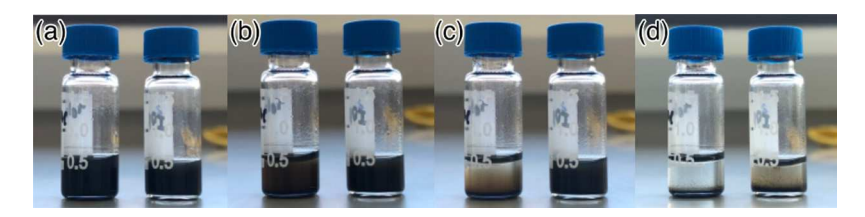


Figure 9. GO dispersed in toluene (left) and isopropyl alcohol (right). Images were taken periodically starting with (a) immediately after dispersion. Unperturbed dispersions were imaged after (b) 10 min, (c) 30 min, and (d) 3 h.

introduced during synthesis may also contribute to the decomposition of OLA. Notably, sulfur is known to reduce the ligand at the vinyl site during synthesis to form a polysulfide, ^{32,33,36,65} which is then shown to form graphitic residue upon annealing under inert conditions. ³⁴

3.5. Partial Graphene Oxide Isolation. In identifying methods to isolate GO, a reduction of the FGL can be achieved prior to the sintering process. Due to the polarity of GO's functional groups, ^{27,47} the flakes will form a heterogeneous mixture with CZTS NCs, in support of our theory illustrated in Scheme 1d. ^{27,47} This allows for an opportunity to isolate the GO prior to deposition, as it is expected that these GOs will readily aggregate and crash out of the nonpolar solvents used to disperse the CZTS NCs.

To isolate the GO, the powdered CZTS NCs were first dispersed in toluene and IPA (1:1). Centrifugation was performed, promoting the dense CZTS NCs to precipitate, while the GO remained dispersed in solvent. Upon supernatant collection, a rotovap was used to dry the precipitate down into a powdered material (see Figure S5). The collection of the GO from the NCs is confirmed by Raman spectroscopy of the collected powdered material (Figure 8a). A high error between 150 and 300 cm⁻¹ is indicative of the residual CZTS; however, compared to the Raman spectrum of CZTS NCs (Figure 3), this CZTS is only present in trace amounts, and the isolated material is primarily composed of GO.

The collected supernatant was subjected to suspension-stability tests in both nonpolar and polar solvents. As OLA-capped CZTS NCs are stable in nonpolar solvents (toluene) and GO's hydroxyl and epoxy groups are more stable in polar solvents (IPA), ^{27,47} it is expected that the GO will readily crash out of solution while in the toluene. Dilute solutions (4 mg/mL) of the isolated material were suspended in toluene and IPA, as shown in Figure 9. While dispersible in toluene, flocculation occurs in toluene; the material aggregates into dense clusters until sedimentation precipitation transpires. This result is apparent within the first 10 min of dispersion (visual opacity gradient), with a majority of the material settling out of solution within 3 h. To affirm that the flocculation results from immiscibility between the polar

functional groups of GO and toluene, the material was also suspended in polar IPA. Consistent with the formation of GO, the material exhibited sufficient stability first 30 min; however, after 3 h, a significant portion of the material had crashed out of the suspension due to GO innate instability in solvent. As such, this section details a method to isolate GO through additional NC washing (centrifugation precipitation).

To monitor the efficacy of GO removal from the final NC material, Raman spectroscopy on the washed powdered material was performed. The resulting spectra in Figure 8b reveal that residual graphitic material is still present within the final NC powder. This remaining graphitic material appears to be structurally consistent with the graphitic material found in the NCs, which were washed twice (Figure 3), and the graphitic material found in the collected supernatant (Figure 8a).

Further, while the supernatant collected from the washing process is primarily graphitic carbon, GDOES profiles within Figure 8c of resulting washed NC films reveal that this isolation only resulted in a small reduction of carbon within the observed FGL (<2%). This offers further evidence that only partial isolation of GO was achieved through the washing methods used in this work, and, the carbonaceous residue that arises from OLA pyrolysis is not solely GO.

4. SUMMARY AND CONCLUSIONS

In this study, we demonstrated that OLA used in the CZTS NC synthesis pyrolyzes into graphitic carbon at temperatures as low as 225 $^{\circ}$ C. Historically, it was expected that this process occurs during high-temperature (500 $^{\circ}$ C) sintering of deposited NC films, where the pyrolyzed ligand would be expelled into a carbon-rich fine-grained layer underneath the active material. However, our findings reveal that OLA pyrolysis occurs during the CZTS NC synthesis at 225 $^{\circ}$ C and is expected to be ubiquitous for NC syntheses that exceed the 200 $^{\circ}$ C decomposition temperature. As a result, this byproduct likely is incorporated into the synthesis of many OLA-based nanomaterials, even if post-thermal treatments are not employed. $^{8-10}$

Furthermore, this graphitic carbon is identified to be nanostructured flakes of disordered GO. To account for these findings, in this work, we proposed an updated mechanism for the decomposition of OLA during NC processing: (i) decomposition into nanostructured GO flakes, (ii) heterogeneous mixture of GO and NCs within the NC ink, and (iii) sedimentation of GO during deposition.

Further, we identify that the source of oxygen is not native to the ligand and that precursor selection is critical for determining the graphitization of the organic ligand. As it is now evident that GO is produced prior to film sintering, alternative low-temperature treatments are utilized to remove this material. Herein, we identify a washing method to partially isolate GO postsynthesis in aims to reduce the FGL within sintered films or remove the byproduct within other OLA-based syntheses.

ASSOCIATED CONTENT

Supporting Information

The Supporting Information is available free of charge at https://pubs.acs.org/doi/10.1021/acs.chemmater.0c03088.

NC size analysis, cross-sectional scanning electron micrographs, additional GDOES data and XPS survey spectra, optical images of the supernatant material, and ¹H NMR of OLA (PDF)

AUTHOR INFORMATION

Corresponding Author

Christine K. Luscombe — Department of Materials Science and Engineering, Molecular Engineering and Sciences Institute, and Department of Chemistry, University of Washington, Seattle, Washington 98195-2120, United States; orcid.org/0000-0001-7456-1343; Email: luscombe@uw.edu

Author

Breena M. Sperry — Department of Materials Science and Engineering, University of Washington, Seattle, Washington 98195-2120. United States

Complete contact information is available at: https://pubs.acs.org/10.1021/acs.chemmater.0c03088

Author Contributions

The manuscript was written through contributions of all authors. All authors have given approval to the final version of the manuscript.

Notes

The authors declare no competing financial interest.

ACKNOWLEDGMENTS

B.M.S. and C.K.L. acknowledge financial support from the National Science Foundation (NSF) Materials Research Science and Engineering Centers (DMR-1719797). Part of this work was conducted at the Molecular Analysis Facility, a National Nanotechnology Coordinated Infrastructure site at the University of Washington, which is supported in part by the National Science Foundation (Grant NNCI-1542101), the University of Washington, the Molecular Engineering & Sciences Institute, and the Clean Energy Institute. The authors also thank Dr. Samantha L. Young of the Molecular Analysis Facility for XPS data acquisition, Tatyana Galenko of Material

Science and Engineering for TGA data acquisition, and Yunping Huang for ¹H NMR data acquisition.

ABBREVIATIONS

CZTS, Cu_2ZnSnS_4 ; CZTSSe, $Cu_2ZnSn(S,Se)_4$; FGL, finegrain layer; GDOES, glow discharge optical emission spectroscopy; GO, graphene oxide; IPA, isopropyl alcohol; LGL, large-grain layer; NC, nanocrystal; OLA, oleylamine; XPS, X-ray photoelectron spectroscopy

REFERENCES

- (1) Rao, C. N. R.; Thomas, P. J.; Kulkarini, G. U. Nanocrystals: Synthesis, Properties and Applications; Springer: Berlin, 2007; pp 25-67
- (2) Wark, M. Solution Processing of Inorganic Materials, 1st ed.; John Wiley & Sons Ltd.: Hoboken, NJ, 2009; pp 313-333.
- (3) Greener, J.; Pearson, G.; Cakmak, M. Roll-to-Roll Manufacturing: Process Elements and Recent Advances, 1st ed.; John Wiley & Sons Ltd.: Hoboken, 2018; pp 1–15.
- (4) Heuer-Jungemann, A.; Feliu, N.; Bakaimi, I.; Hamaly, M.; Alkilany, A.; Chakraborty, I.; Masood, A.; Casula, M. F.; Kostopoulou, A.; Oh, E.; Susumu, K.; Stewart, M. H.; Medintz, I. L.; Stratakis, E.; Parak, W. J.; Kanaras, A. G. The Role of Ligands in the Chemical Synthesis and Applications of Inorganic Nanoparticles. *Chem. Rev.* 2019, 119, 4819–4880.
- (5) Phan, C. M.; Nguyen, H. M. Role of Capping Agent in Wet Synthesis of Nanoparticles. J. Phys. Chem. A 2017, 121, 3213-3219.
- (6) Boles, M. A.; Ling, D.; Hyeon, T.; Talapin, D. V. The Surface Science of Nanocrystals. *Nat. Mater.* **2016**, *15*, 141–153.
- (7) Mourdikoudis, S.; Liz-Marzán, L. M. Oleylamine in Nanoparticle Synthesis. *Chem. Mater.* **2013**, *25*, 1465–1476.
- (8) Salavati-Niasari, M.; Davar, F.; Mazaheri, M.; Shaterian, M. Preparation of Cobalt Nanoparticles from [Bis(Salicylidene)Cobalt-(II)]-Oleylamine Complex by Thermal Decomposition. *J. Magn. Magn. Mater.* **2008**, 320, 575–578.
- (9) Huang, X.; Parashar, V. K.; Gijs, M. A. M. Nucleation and Growth Behavior of CdSe Nanocrystals Synthesized in the Presence of Oleylamine Coordinating Ligand. *Langmuir* **2018**, *34*, 6070–6076.
- (10) Salavati-Niasari, M.; Davar, F.; Mazaheri, M. Preparation of ZnO Nanoparticles from [Bis(Acetylacetonato)Zinc(II)]-Oleylamine Complex by Thermal Decomposition. *Mater. Lett.* **2008**, *62*, 1890–1892.
- (11) Martin, T. R.; Katahara, J. K.; Bucherl, C. N.; Krueger, B. W.; Hillhouse, H. W.; Luscombe, C. K. Nanoparticle Ligands and Pyrolized Graphitic Carbon in CZTSSe Photovoltaic Devices. *Chem. Mater.* **2016**, 28, 135–145.
- (12) Bucherl, C. N.; Oleson, K. R.; Hillhouse, H. W. Thin Film Solar Cells from Sintered Nanocrystals. *Curr. Opin. Chem. Eng.* **2013**, *2*, 168–177.
- (13) Magdassi, S.; Grouchko, M.; Berezin, O.; Kamyshny, A. Triggering the Sintering of Silver Nanoparticles at Room Temperature. ACS Nano 2010, 4, 1943–1948.
- (14) Aigner, W.; Bienek, O.; Falcão, B. P.; Ahmed, S. U.; Wiggers, H.; Stutzmann, M.; Pereira, R. N. Intra- and Inter-Nanocrystal Charge Transport in Nanocrystal Films. *Nanoscale* **2018**, *10*, 8042–8057.
- (15) Cao, Y.; Denny, M. S.; Caspar, J. V.; Farneth, W. E.; Guo, Q.; Ionkin, A. S.; Johnson, L. K.; Lu, M.; Malajovich, I.; Radu, D.; Rosenfeld, H. D.; Choudhury, K. R.; Wu, W. High-Efficiency Solution-Processed Cu₂ZnSn(S,Se)₄ Thin-Film Solar Cells Prepared from Binary and Ternary Nanoparticles. *J. Am. Chem. Soc.* **2012**, *134*, 15644–15647.
- (16) Wu, W.; Cao, Y.; Caspar, J. V.; Guo, Q.; Johnson, L. K.; Malajovich, I.; Rosenfeld, H. D.; Choudhury, K. R. Studies of the Fine-Grain Sub-Layer in the Printed CZTSSe Photovoltaic Devices. *J. Mater. Chem. C* **2014**, *2*, 3777–3781.
- (17) Mainz, R.; Walker, B. C.; Schmidt, S. S.; Zander, O.; Weber, A.; Rodriguez-Alvarez, H.; Just, J.; Klaus, M.; Agrawal, R.; Unold, T. Real-Time Observation of Cu₂ZnSn(S,Se)₄ Solar Cell Absorber Layer

Formation from Nanoparticle Precursors. Phys. Chem. Chem. Phys. 2013, 15, 18281–18289.

- (18) Guo, Q.; Ford, G. M.; Yang, W. C.; Walker, B. C.; Stach, E. A.; Hillhouse, H. W.; Agrawal, R. Fabrication of 7.2% Efficient CZTSSe Solar Cells Using CZTS Nanocrystals. *J. Am. Chem. Soc.* **2010**, *132*, 17384–17386.
- (19) Williams, B. A.; Smeaton, M. A.; Trejo, N. D.; Francis, L. F.; Aydil, E. S. Effect of Nanocrystal Size and Carbon on Grain Growth during Annealing of Copper Zinc Tin Sulfide Nanocrystal Coatings. *Chem. Mater.* **2017**, *29*, 1676–1683.
- (20) Hages, C. J.; Koeper, M. J.; Miskin, C. K.; Brew, K. W.; Agrawal, R. Controlled Grain Growth for High Performance Nanoparticle-Based Kesterite Solar Cells. *Chem. Mater.* **2016**, 28, 7703–7714.
- (21) Clark, J. A.; Uhl, A. R.; Martin, T. R.; Hillhouse, H. W. Evolution of Morphology and Composition during Annealing and Selenization in Solution-Processed Cu₂ZnSn(S,Se)₄. *Chem. Mater.* **2017**, 29, 9328–9339.
- (22) Engberg, S.; Canulescu, S.; Schou, J. Liquid Phase Assisted Grain Growth in $\text{Cu}_2\text{ZnSnS}_4$ Nanoparticle Thin Films by Alkali Element Incorporation. *RSC Adv.* **2018**, *8*, 7152–7158.
- (23) Miskin, C. K.; Yang, W.-C.; Hages, C. J.; Carter, N. J.; Joglekar, C. S.; Stach, E. A.; Agrawal, R. 9.0% Efficient Cu₂ZnSn(S,Se)₄ Solar Cells from Selenized Nanoparticle Inks. *Prog. Photovoltaics* **2014**, 23, 654–659.
- (24) Chernomordik, B. D.; Béland, A. E.; Deng, D. D.; Francis, L. F.; Aydil, E. S. Microstructure Evolution and Crystal Growth in Cu₂ZnSnS₄ Thin Films Formed by Annealing Colloidal Nanocrystal Coatings. *Chem. Mater.* **2014**, *26*, 3191–3201.
- (25) Mohapatra, P.; Shaw, S.; Mendivelso-Perez, D.; Bobbitt, J. M.; Silva, T. F.; Naab, F.; Yuan, B.; Tian, X.; Smith, E. A.; Cademartiri, L. Calcination Does Not Remove All Carbon from Colloidal Nanocrystal Assemblies. *Nat. Commun.* **2017**, *8*, No. 2038.
- (26) Fichthorn, K. A.; Miron, R. A. Thermal Desorption of Large Molecules from Solid Surfaces. *Phys. Rev. Lett.* **2002**, *89*, No. 196103.
- (27) Dreyer, D. R.; Park, S.; Bielawski, C. W.; Ruoff, R. S. The Chemistry of Graphene Oxide. *Chem. Soc. Rev.* **2010**, 39, 228–240.
- (28) Liu, Z.; Niu, S.; Wang, N. Oleylamine-Functionalized Graphene Oxide as an Electron Block Layer towards High-Performance and Photostable Fullerene-Free Polymer Solar Cells. *Nanoscale* **2017**, *9*, 16293—16304.
- (29) Ha, E.; Liu, W.; Wang, L.; Man, H. W.; Hu, L.; Tsang, S. C. E.; Chan, C. T. L.; Kwok, W. M.; Lee, L. Y. S.; Wong, K. Y. Cu₂ZnSnS₄/MoS₂-Reduced Graphene Oxide Heterostructure: Nanoscale Interfacial Contact and Enhanced Photocatalytic Hydrogen Generation. *Sci. Rep.* **2017**, *7*, No. 39411.
- (30) Togashi, T.; Nakayama, M.; Hashimoto, A.; Ishizaki, M.; Kanaizuka, K.; Kurihara, M. Solvent-Free Synthesis of Monodisperse Cu Nanoparticles by Thermal Decomposition of an Oleylamine-Coordinated Cu Oxalate Complex. *Dalton Trans.* **2018**, *47*, 5342–5347.
- (31) Monfared, A. H.; Zamanian, A.; Beygzadeh, M.; Sharifi, I.; Mozafari, M. A Rapid and Efficient Thermal Decomposition Approach for the Synthesis of Manganese-Zinc/Oleylamine Core/Shell Ferrite Nanoparticles. *J. Alloys Compd.* **2017**, 693, 1090–1095.
- (32) Thomson, J. W.; Nagashima, K.; MacDonald, P. M.; Ozin, G. A. From Sulfur-Amine Solutions to Metal Sulfide Nanocrystals: Peering into the Oleylamine-Sulfur Black Box. *J. Am. Chem. Soc.* **2011**, 133, 5036–5041.
- (33) Kim, E. T.; Chung, W. J.; Lim, J.; Johe, P.; Glass, R. S.; Pyun, J.; Char, K. One-Pot Synthesis of PbS NP/Sulfur-Oleylamine Copolymer Nanocomposites via the Copolymerization of Elemental Sulfur with Oleylamine. *Polym. Chem.* **2014**, *5*, 3617–3623.
- (34) Huang, T. J.; Yin, X.; Tang, C.; Qi, G.; Gong, H. Influence of Ligands on the Formation of Kesterite Thin Films for Solar Cells: A Comparative Study. *ChemSusChem* **2016**, *9*, 1032–1041.
- (35) Dierick, R.; Van Den Broeck, F.; De Nolf, K.; Zhao, Q.; Vantomme, A.; Martins, J. C.; Hens, Z. Surface Chemistry of CuInS2

- Colloidal Nanocrystals, Tight Binding of L-Type Ligands. Chem. Mater. 2014, 26, 5950–5957.
- (36) Lynch, M. An Investigation of Solutions of Sulfur in Oleylamine by Raman Spectroscopy and Their Relation to Lead Sulfide Quantum Dot Synthesis. Undergraduate Honors Thesis; University of Colorado: Boulder, 2017.
- (37) Baranov, D.; Lynch, M. J.; Curtis, A. C.; Carollo, A. R.; Douglass, C. R.; Mateo-Tejada, A. M.; Jonas, D. M. Purification of Oleylamine for Materials Synthesis and Spectroscopic Diagnostics for Trans Isomers. *Chem. Mater.* **2019**, *31*, 1223–1230.
- (38) Asomaning, J.; Mussone, P.; Bressler, D. C. Thermal Deoxygenation and Pyrolysis of Oleic Acid. *J. Anal. Appl. Pyrolysis* **2014**, *105*, 1–7.
- (39) Ferrari, A. C. Raman Spectroscopy of Graphene and Graphite: Disorder, Electron-Phonon Coupling, Doping and Nonadiabatic Effects. *Solid State Commun.* **2007**, *143*, 47–57.
- (40) Childres, I.; Jauregui, L. A.; Park, W.; Cao, H.; Chen, Y. P. Raman Spectroscopy of Graphene and Related Materials. In *New Developments in Photon and Materials Research*; Nova Science Publishers: Hauppauge, NY, 2013; pp 403–418.
- (41) Merlen, A.; Buijnsters, J. G.; Pardanaud, C. A Guide to and Review of the Use of Multiwavelength Raman Spectroscopy for Characterizing Defective Aromatic Carbon Solids: From Graphene to Amorphous Carbons. *Coatings* **2017**, *7*, 153–208.
- (42) Wu, J. B.; Lin, M. L.; Cong, X.; Liu, H. N.; Tan, P. H. Raman Spectroscopy of Graphene-Based Materials and Its Applications in Related Devices. *Chem. Soc. Rev.* **2018**, *47*, 1822–1873.
- (43) Chu, P. K.; Li, L. Characterization of Amorphous and Nanocrystalline Carbon Films. *Mater. Chem. Phys.* **2006**, *96*, 253–277.
- (44) Zheng, P.; Wu, N. Fluorescence and Sensing Applications of Graphene Oxide and Graphene Quantum Dots: A Review. *Chem. Asian J.* **2017**, *12*, 2343–2353.
- (45) Hong, J.; Park, M. K.; Lee, E. J.; Lee, D.; Hwang, D. S.; Ryu, S. Origin of New Broad Raman D and G Peaks in Annealed Graphene. *Sci. Rep.* **2013**, *3*, No. 2700.
- (46) Schwan, J.; Ulrich, S.; Batori, V.; Ehrhardt, H.; Silva, S. R. P. Raman Spectroscopy on Amorphous Carbon Films. *J. Appl. Phys.* **1996**, *80*, 440–447.
- (47) Dave, K.; Park, K. H.; Dhayal, M. Two-Step Process for Programmable Removal of Oxygen Functionalities of Graphene Oxide: Functional, Structural and Electrical Characteristics. *RSC Adv.* **2015**, *5*, 95657–95665.
- (48) Cançado, L. G.; Takai, K.; Enoki, T.; Endo, M.; Kim, Y. A.; Mizusaki, H.; Jorio, A.; Coelho, L. N.; Magalhães-Paniago, R.; Pimenta, M. A. General Equation for the Determination of the Crystallite Size La of Nanographite by Raman Spectroscopy. *Appl. Phys. Lett.* **2006**, *88*, No. 163106.
- (49) Tuinstra, F.; Koenig, J. L. Raman Spectrum of Graphite. *J. Chem. Phys.* **1970**, 53, 1126–1130.
- (50) Yang, K.; Liang, S.; Zou, L.; Huang, L.; Park, C.; Zhu, L.; Fang, J.; Fu, Q.; Wang, H. Intercalating Oleylamines in Graphite Oxide. *Langmuir* **2012**, 28, 2904–2908.
- (51) Bhuyan, M. S. A.; Uddin, M. N.; Islam, M. M.; Bipasha, F. A.; Hossain, S. S. Synthesis of Graphene. *Int. Nano Lett.* **2016**, *6*, 65–83.
- (52) Obraztsov, A. N.; Obraztsova, E. A.; Tyurnina, A. V.; Zolotukhin, A. A. Chemical Vapor Deposition of Thin Graphite Films of Nanometer Thickness. *Carbon* **2007**, *45*, 2017–2021.
- (53) Wang, J. J.; Zhu, M. Y.; Outlaw, R. A.; Zhao, X.; Manos, D. M.; Holloway, B. C.; Mammana, V. P. Free-Standing Subnanometer Graphite Sheets. *Appl. Phys. Lett.* **2004**, *85*, 1265–1267.
- (54) Xia, C.; Zhu, S.; Feng, T.; Yang, M.; Yang, B. Evolution and Synthesis of Carbon Dots: From Carbon Dots to Carbonized Polymer Dots. *Adv. Sci.* **2019**, *6*, No. 1901316.
- (55) Hsu, P. C.; Chen, P. C.; Ou, C. M.; Chang, H. Y.; Chang, H. T. Extremely High Inhibition Activity of Photoluminescent Carbon Nanodots toward Cancer Cells. *J. Mater. Chem. B* **2013**, *1*, 1774–1781.

- (56) Dai, B.; Wu, C.; Lu, Y.; Deng, D.; Xu, S. Synthesis and Formation Mechanism of S-Doped Carbon Dots from Low-Molecule-Weight Organics. *J. Lumin.* **2017**, *190*, 108–114.
- (57) Zhou, L.; Geng, J.; Liu, B. Graphene Quantum Dots from Polycyclic Aromatic Hydrocarbon for Bioimaging and Sensing of Fe³⁺ and Hydrogen Peroxide. *Part. Part. Syst. Charact.* **2013**, *30*, 1086–1092.
- (58) Kubátová, A.; Ŝávová, J.; Seames, W. S.; Luo, Y.; Sadrameli, S. M.; Linnen, M. J.; Baglayeva, G. V.; Smoliakova, I. P.; Kozliak, E. I. Triacylglyceride Thermal Cracking: Pathways to Cyclic Hydrocarbons. *Energy Fuels* **2012**, *26*, 672–685.
- (59) Tiong, V. T.; Zhang, Y.; Bell, J.; Wang, H. Carbon Concentration Dependent Grain Growth of Cu₂ZnSnS₄ Thin Films. *RSC Adv.* **2015**, *5*, 20178–20185.
- (60) Sadezky, A.; Muckenhuber, H.; Grothe, H.; Niessner, R.; Pöschl, U. Raman Microspectroscopy of Soot and Related Carbonaceous Materials: Spectral Analysis and Structural Information. *Carbon* **2005**, *43*, 1731–1742.
- (61) Achten, C.; Andersson, J. T. Overview of Polycyclic Aromatic Compounds (PAC). *Polycyclic Aromat. Compd.* **2015**, *35*, 177–186.
- (62) Min, Y.; He, G.; Xu, Q.; Chen, Y. Self-Assembled Encapsulation of Graphene Oxide/Ag@AgCl as a Z-Scheme Photocatalytic System for Pollutant Removal. *J. Mater. Chem. A* **2014**, *2*, 1294–1301.
- (63) Ederer, J.; Janoš, P.; Ecorchard, P.; Tolasz, J.; Štengl, V.; Beneš, H.; Perchacz, M.; Pop-Georgievski, O. Determination of Amino Groups on Functionalized Graphene Oxide for Polyurethane Nanomaterials: XPS Quantitation vs. Functional Speciation. *RSC Adv.* 2017, 7, 12464–12473.
- (64) Wilson, D.; Langell, M. A. XPS Analysis of Oleylamine/Oleic Acid Capped Fe 3 O 4 Nanoparticles as a Function of Temperature. *Appl. Surf. Sci.* **2014**, *303*, 6–13.
- (65) Zhang, Y.; Glass, R. S.; Char, K.; Pyun, J. Recent Advances in the Polymerization of Elemental Sulphur, Inverse Vulcanization and Methods to Obtain Functional Chalcogenide Hybrid Inorganic/Organic Polymers (CHIPs). *Polym. Chem.* **2019**, *10*, 4078–4105.